Special Issue Article

The application of body scanning, numerical simulations and wind tunnel testing for the aerodynamic development of cyclists

Shian Chi[1] (iD)**, John Pitman[2], Tim Crouch[1]** (iD)**, David Burton[1] and Mark Thompson[1]**

Abstract

The aerodynamic efficiency of an elite cyclist is often evaluated and optimised using either one or a combination of field testing, wind-tunnel testing and numerical simulation. This study focuses on the processes and limitations involved in using a body scan to produce an accurate geometry for input to numerical simulation, with validation through drag comparisons from wind-tunnel tests and vortical wake-flow features reported in previous experimental studies. Transitional Shear Stress Transport Reynolds-Averaged Navier-Stokes simulations based on the scanned geometry were undertaken for a 180° half crank cycle at 15° increments. The sectional drag force contributions of 23 body subparts are presented, documenting the contribution and variation of each body/cycle component over the cycle. These methods are evaluated and the limitations of the approaches are discussed. The results from the numerical simulation and the wind tunnel measured drag force were very similar, differing by approximately 1%–7% for various crank angles.

Introduction

In elite cycling, the main contribution to the resistive force is aerodynamic drag, making up more than 90% of the total. Of that, approximately 30% is due to the bike components with the remaining approximately 70% due to the rider.[1–3] Thus, aerodynamic efficiency plays a very important role and it can be improved by reducing either the drag coefficient or the frontal area to give cyclists a competitive advantage.

To evaluate the aerodynamic performance of cyclists, both wind-tunnel testing and computational fluid dynamics (CFD) are often used. Often, a majority of testing is done in wind tunnels, with CFD used as an additional tool to provide the fully detailed flow around cyclists. Knowledge of the detailed flow field can allow targeted modifications to be made to improve the aerodynamic performance. However, due to the complex geometry involved, previous studies have often used simplified models of cyclists/bicycles or simply just a cyclist modelled in CFD.

The cyclist/bicycle combination can be considered to be a bluff body as a whole. Even so, it consists of a number of bluff/aerodynamic components, such as

aerofoil-profiled elements of the bicycle frame and tapered cylinder-like geometries of the arms and thighs.[4–6] Furthermore, both the geometry and aerodynamics become more complex as dynamic pedalling is introduced. The overall complexity demands significant computational resources to produce a model with good fidelity.

Recently, Griffith et al.[4] conducted numerical simulations based on a computer-aided design model of a cyclist/bicycle combination for a 0°–180° crank sweep, but subject to fixed leg positions at each specific crank angle tested. Both steady-state and transient simulations were performed based on the $k - \omega$ Reynolds-Averaged Navier-Stokes (RANS) and the Scale-Adaptive

[1]Department of Mechanical and Aerospace Engineering, Monash University, Clayton, VIC, Australia
[2]Cycling Australia, Adelaide, SA, Australia

Corresponding author:
Shian Chi, Department of Mechanical and Aerospace Engineering, Monash University, Clayton, VIC 3800, Australia.
Email: Shian.Chi@monash.edu

Simulation (SAS) Shear Stress Transport (SST) model, respectively. The drag prediction trend with leg position matched wind-tunnel measurements, reproducing the observed cyclic variation well, but the curves were offset by approximately 13%–17%. The full-scale CFD model used approximately 33 million computational cells, indicative of the large size of the computation.

Further numerical studies of cyclists have been conducted by Defraeye et al.[7] based on a scale model of a cyclist, but replacing the bike with an aerofoil. A variety of RANS simulations were conducted to understand the performance of different turbulence models, with the SST $k - \omega$ model found to achieve reasonable results as assessed by matching against wind-tunnel drag, lift and pitch measurements. Furthermore, Defraeye et al.[7] performed simulations of the flow around a cyclist subject to static leg position by employing both steady-state RANS simulations using the $k - \epsilon$ model and the large eddy simulation (LES) approach. However, the assumption was made that the total drag contributed by the bike and rider combination was comparable to only the cyclist, an assumption that was difficult to test. However, the pressure correlation between the two was satisfactory. A recent numerical study has been conducted on more than one cyclist that included cycling peloton consisting of 121 cyclists by Blocken et al.[8] using RANS Transition SST model validated by wind tunnel testing. Also, Blocken et al.[9] has conducted a CFD study of two drafting cyclists in the upright position (UP), dropped position (DP) and time-trial position (TTP) that were supported by wind tunnel tests. For the wind tunnel tests, the cyclist was scanned and three-dimensionally (3D) printed.

In this study, the authors aim to provide a case study of the application of the full process from scanning to numerical simulation applied to a mannequin for the purpose of characterising both the benefits and the challenges of the current techniques. While moving leg models and hybrid-LES methods are available, the complexity in accurately modelling the dynamic geometry and the computational cost of these simulations mean that it is still far more common to apply less complex methods, such as steady simulations, for cyclist aerodynamic performance development. The intention is, therefore, to demonstrate the full process and both the benefits and shortcomings of the approach.

In order to validate the numerical model, wind-tunnel tests were conducted on a cyclist/bicycle combination for a $0°$–$360°$ crank angle sweep at $15°$ pedal position increments. To conduct matching numerical simulations, a body scan of the cyclist/bicycle combination was undertaken to capture the actual surface geometry, in order to provide a realistic reproduction of the pair to build a geometrically accurate numerical model. The reconstructed scan data were further processed and segmented to allow the legs to adjust as the pedal position was changed. Using this model, simulations were conducted for $0°$–$180°$ crank angle at $15°$ increments, matching the experiments over the first half of the cycle. This allowed for numerical modelling and the drag predictions of this were assessed with direct wind-tunnel measurements. In addition, the wake-flow structures were compared with previous experiments by Crouch et al.[10] To provide further validation of the body scan data, further processing provided geometric measurements, such as frontal area, torso angle and other important parameters of the cyclist–bicycle combination, which could be directly compared with measurements of the wind-tunnel pair. One of the project's wider aims was to develop this process into a reliable stand-alone numerical optimisation tool.

Methodology

To perform CFD simulations over the $0°$–$180°$ crank sweep for cyclist/bicycle combination, it was necessary to first scan the actual rider/bicycle combination, followed by post-processing the derived surface geometry to be compatible with variable leg position CFD simulations. To provide validation for the CFD model, experiments were undertaken in the Monash University 1.4 MW wind tunnel for the rider/bicycle combination with leg position varied over the $0°$–$360°$ crank cycle. The details of this process are provided in the following three subsections. How the scan was conducted using a structured-light scanner is described in Section 'Body scan'. Section 'Experiments' provides the experimental methodology for wind-tunnel testing, and a detailed description of the numerical methodology is given in Section 'Numerical methodology'.

Body scan

The body scan was conducted using a structured-light, 3D scanner: the *Artec Eva*. The geometry setup in the wind tunnel and the reconstructed geometry based on the scan data are shown in Figures 1 and 2. Initially, surface sections of the cyclist/bicycle were scanned using the hand-held scanner. Following this, these overlapping surfaces were aligned with each other using *Artec Studio 10* (AS-10) software. The surfaces are represented as triangular meshes; the scanning operation for the bicycle and cyclist consisted of 140 and 64 individual scans, respectively. The majority of scans overlapped with others to aid reconstruction. Another software application, *Mesh Mixer*, was utilised to simplify the crank and improve the mesh.

Next, the triangular surface mesh was converted to a NURBS (Non-Uniform Rational B-Spline) surface representation. To accomplish this, *Geomagic Design X* was used to fit polynomial splines. Once this stage was completed, the processed scan geometry was imported into the CAD package *SolidWorks* to align the model to the respective x, y, z coordinate system, and then the model was parameterized to allow leg movement consistent with variable crank position. In addition, the crank and pedals were included and the fluid domain
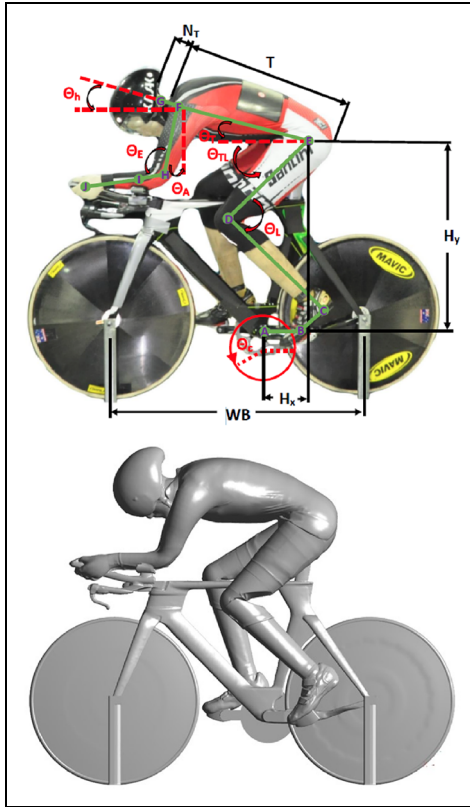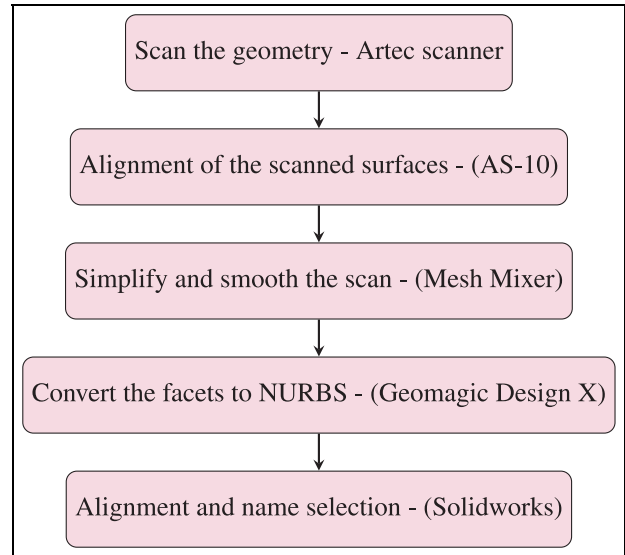
Figure 1. The top figure shows the side view of the cyclist from the wind-tunnel setup and the bottom figure shows the scan-derived surface of the cyclist/bicycle combination for use with the CFD modelling.
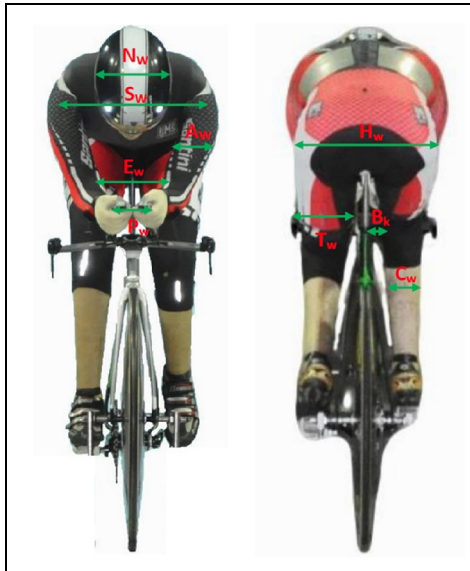
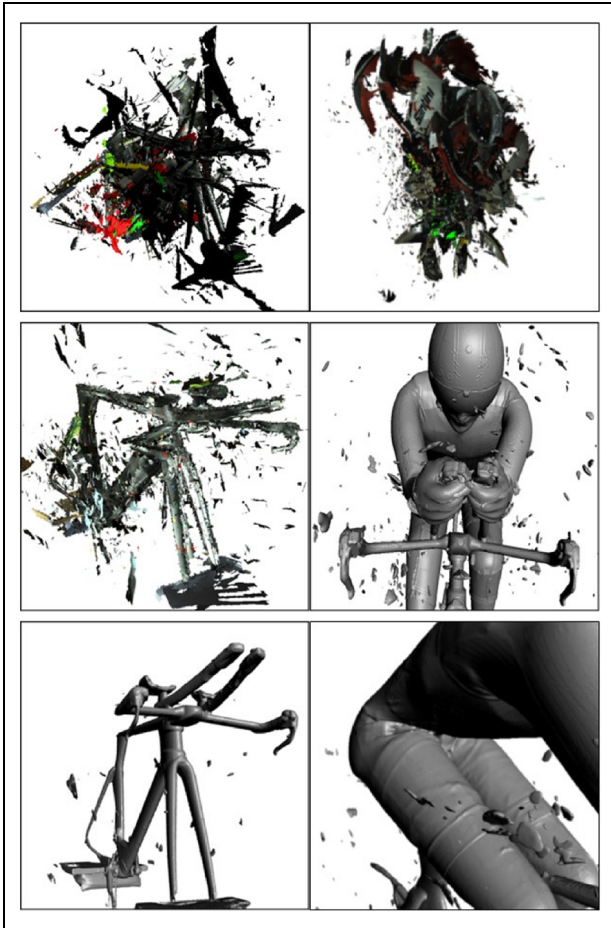**Figure 2.** Left and right images show front and back views of the cyclist in the wind tunnel.

Figure 3. Steps involved in taking the body scan to the surface mesh for the numerical modelling.

geometry are shown in Figure 4, conversion of the facets to NURBS is shown in Figure 5 and the addition of named elements is shown in Figure 6. Subsequently, this model was imported into the mesh generation package *SpaceClaim 18.0*, prior to simulating the flow using the numerical CFD software *Fluent* from the *ANSYS 18.0* package. The details of the process taking the scan input to the CAD output is presented in Section 'Body scan fidelity'.

Experiments

The cyclist/bicycle combination was tested in the 1.4 MW wind tunnel at Monash University. The reason for choosing a mannequin rather than an actual athlete was due to difficulties in repeatability, attributable to not being able to maintain a consistent body posture for a prolonged duration, for example, as previously described for athlete testing undertaken by Barry et al.[11] The mannequin was manufactured based on an idealisation of an approximate body shape with dimensions typical of an elite track cyclist from the *Australian Institute of Sport*. The mannequin was constructed in such a way that it allowed the full range of motion about the knee and hip when mounted on a generic time-trial bicycle.

The turbulence intensity in the open-jet wind tunnel was measured at 1.6% and the blockage was less than 4%. A six-component *Kistler* force balance of the piezoelectric type was used to measure the lift and drag forces experienced by the mannequin/bicycle combination. Force measurements were low-pass filtered at approximately 10 Hz, taken as the mean of three separate tests, each sampled at 1000 Hz for 45 s. The uncertainty/repeatability of the drag-area measurements was better than $\pm 0.0005 \, m^2$.

was added based on the cyclist/bicycle surface geometry. This process is depicted in the flow chart (shown in Figure 3). Furthermore, to provide a visual overview of the process, the scanned surfaces and overall simplified

Figure 4. The top figures show views of the acquired scan surfaces; the middle figures show aligned surfaces still containing considerable noise; and the bottom figures show views of the images after clean up with *Artec Studio 10*.

All simulations were conducted subject to a free-stream velocity of 60 km/h, matching typical elite-cycling speeds over the final stages of road races. Figures 1 and 2 represent the cyclist/bicycle combination in the wind tunnel and for the CFD simulations.
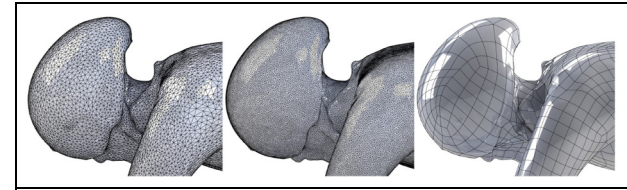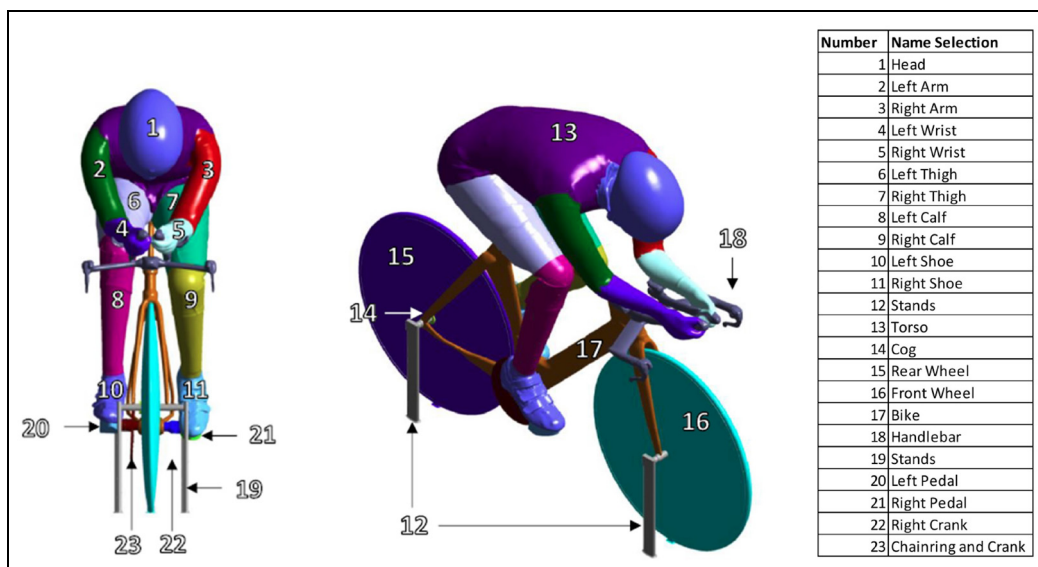

Figure 5. The left image shows the reduced mesh; the middle images shows the original scanned mesh; and the right image shows the reduced mesh converted to NURBS.

The 0° crank angle, taken as a reference angle, corresponds to where the pedals are level horizontally with the right foot towards the stream-wise direction. Figure 1 shows this reference position.

Numerical methodology

Geometry. The cyclist/bicycle combination for the CFD model was reconstructed using a body scan from the setup in the wind tunnel. The cyclist/bicycle surface was segmented, allowing contributions to the overall resistive force of 23 sub-body components to be monitored for each crank angle (see Figure 6). This detailed parameterization of the model was undertaken to allow detailed dynamic CFD simulations and analysis, especially for future studies. The 3D geometry had dimensions shown in Table 1 and Figure 7. A generic bike was scanned separately to incorporate into the overall cyclist/bicycle model. A detailed evaluation of the final scan with respect to the setup is discussed in Section 'Body scan fidelity'.

Domain and boundary conditions. The full-scale cyclist/ bicycle combination was positioned in the computational domain, with the origin defined at the bottom centre of the domain inlet as illustrated in Figure 8. It was meshed with hexahedral cells as shown in Figures 9

| Number	Name Selection
1	Head
2	Left Arm
3	Right Arm
4	Left Wrist
5	Right Wrist
6	Left Thigh
7	Right Thigh
8	Left Calf
9	Right Calf
10	Left Shoe
11	Right Shoe
12	Stands
13	Torso
14	Cog
15	Rear Wheel
16	Front Wheel
17	Bike
18	Handlebar
19	Stands
20	Left Pedal
21	Right Pedal
22	Right Crank
23	Chainring and Crank

Figure 6. Segmentation of the cyclist/bicycle surface used to record contributions to drag.

Table 1. Wind-tunnel/CFD model and setup dimensions.

Name	Symbol	Standard position
Crank angle	θ	0 °–360 ° in 15 ° increments
Hip angle	θ_{TL}	$f(\theta_C)$
Knee angle	θ_L	$f(\theta_C)$
Torso angle	θ_T	13 °
Upper arm angle	θ_A	26 °
Elbow angle	θ_E	120 °
Head angle	θ_H	6 °

| Name	Symbol	Length (mm)
Head gap	N_T	10
Hip location (x)	H_x	200
Hip location (y)	H_y	806
Wheel base	WB	1010
Chord length – torso	T	640
Torso	$E \rightarrow F$	485
Crank	$A \rightarrow B$	175
Pedal – heel bone	$B \rightarrow C$	142
Heel bone – knee	$C \rightarrow D$	536
Thigh	$D \rightarrow E$	480
Upper arm	$F \rightarrow H$	300
Elbow – elbow pad	$H \rightarrow I$	84
Elbow pad – fist	$I \rightarrow J$	323
Helmet width	N_w	204
Shoulder width	S_w	225
Mid-arm diameter	A_w	116
Upper-leg diameter	T_w	180
Calf diameter	C_w	98
Elbow gap	E_w	113
Top tube – knee	B_k	5
Hip width	H_w	372
Handle bar gap	P_w	53

CFD: computational fluid dynamics.
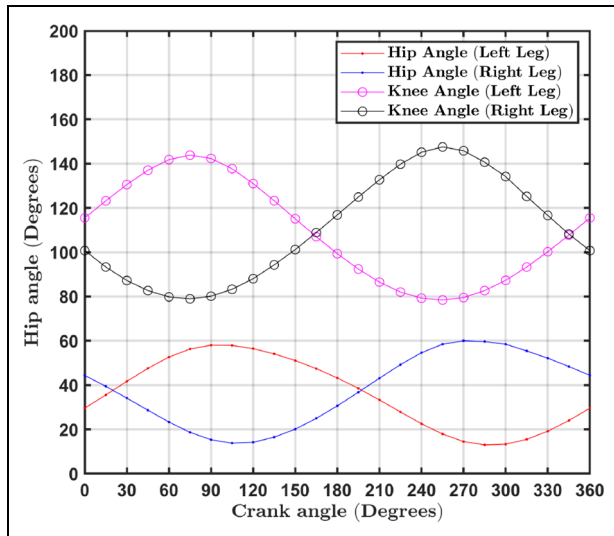
Figure 7. Left and right hip and knee angles as a function of crank angle.

and 10. The dimensions of the domain are normalised by the wheel base (*D*) of the bicycle in each of the *x, y, z* directions, corresponding to streamwise, spanwise and vertical directions, receptively.
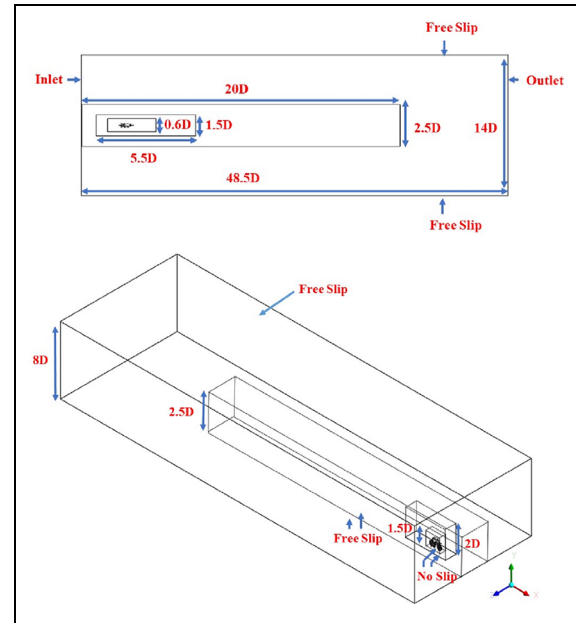

Figure 8. Schematic of the computational domain showing dimensions, placement of the cyclist, refinement boxes and boundary conditions.

At the inlet, a uniform velocity of 60 km/h was applied, subject to a turbulence intensity of 1.6% to replicate the background level of the wind-tunnel environment. The Reynolds number based on the torso cord length, *T*, was 7.4×10^5. This corresponds to an equivalent Reynolds number based on the upper arm width of 1.2×10^5. A no-slip boundary condition was applied to the cyclist and the splitter plate, with the latter having dimensions of $5.5D \times 1.5D$. The splitter plate was used to allow some control over the boundary layer development at the ground surface. Over the remaining bottom domain boundary, again a free-slip condition was applied. For the outlet boundary, zero static pressure was applied, and for the sides and top boundaries, a free-slip boundary condition was used. These conditions are illustrated in Figure 8.

Numerical solver and meshing strategy. The numerical domain was meshed using *Fluent meshing* and the flow field was solved using *ANSYS Fluent 18.0*. Hexahedral cells were primarily used for the mesh. This mesh was structured to use a high concentration of fine cells near the geometry surface with a smooth transition moving away. *Inflation layers* were used on the splitter plate and the bike to accurately capture the boundary layer variation. To the authors' knowledge, this is also the first attempt to use a contact patch to connect the wheels and ground; other studies employed a gap.[4,7] For this study, three refinement zones of increasing fineness were used to accurately capture the velocity field near the cyclist. This meshing strategy was based on a set of initial simulations used to determine an
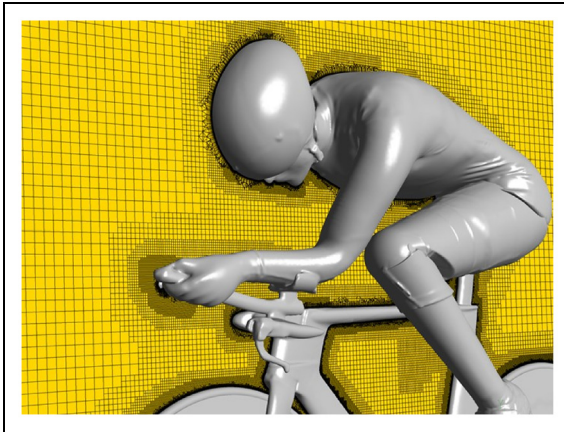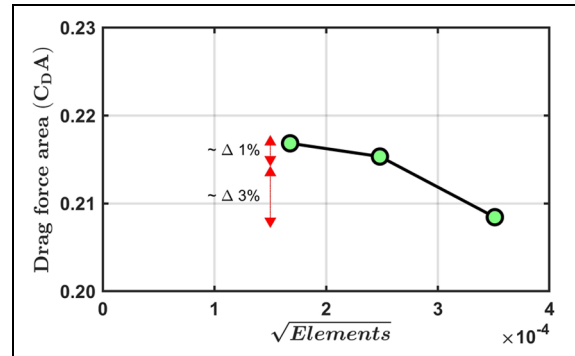
Figure 9. Non-conformal hexahedral mesh in the vicinity of the cyclist/bicycle combination for the fine mesh case.
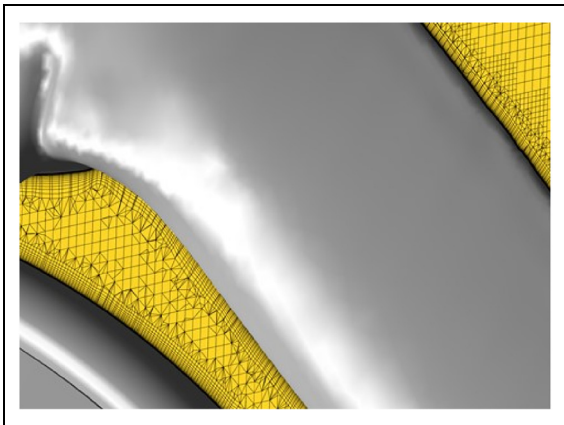
Figure 10. Close-up view of the front fork and wheel, showing the 20 *inflation layers* used to capture the boundary layer for the fine mesh.

Figure 11. Dependence on drag-area coefficient on mesh resolution for the 15 ° crank-angle case.

approximate mesh point concentration required to capture the flow features. Three meshes were then constructed: coarse, medium and fine. The convergence criterion for solving each of the equations was set at 10^{-4}. A convergence study was carried out based on these three configurations, with mesh characteristics shown in Table 2. Those sizings were based on the streamwise hip location (L). The coarse, medium and fine meshes contained approximately 8, 16 and 36 million cells, respectively. The result of the convergence study showed a less than 1% difference between the medium- and fine-mesh predictions of the drag for the 15° crank angle case (see Figure 11). Despite this, the fine mesh was chosen for the remaining simulations.

The flows were simulated using the steady-state RANS transitional shear stress transport (TSST) turbulence model over the 0°–180° crank cycle at 15° increments. The usage of the TSST mode was due to the fact that flow transition in the boundary layer occurs from laminar to turbulent flow at a Reynolds number close to that studied. The cyclist's body components, such as the arms, calves and thighs, represent cylinder-like geometries that have been represented that way by some authors.[4,6] According to Underwood,[5] typical Reynolds numbers around the arm can vary between $0.66 \times 10^5 < \mathrm{Re} < 1.15 \times 10^5$, thighs $1.17 \times 10^5 < \mathrm{Re} < 2.05 \times 10^5$ and calf $0.73 \times 10^5 < \mathrm{Re} < 1.28 \times 10^5$. Furthermore, the authors of the model recommend using the TSST turbulence model in the drag crisis regions.[12]

For the initial phase with the results presented in this article, RANS simulations were undertaken. RANS has been the most widely used turbulence modelling approach. With it, the Navier-Stokes equations are split into mean and fluctuating components. The total velocity (u_i) is a linear combination of the mean velocity ($\overline{u}_i$) and the fluctuating velocity, (u_i')

Table 2. Mesh independence study for the coarse, medium and fine options.

Parameters	Coarse	Medium	Fine
Far-field refinement	$0.020 - 3.20L$	$0.013 - 2.40L$	$0.009 - 1.60L$
Near wake refinement 1	$0.20L$	$0.15L$	$0.10L$
Near wake refinement 2	$0.40L$	$0.30L$	$0.20L$
Far wake refinement	$0.55L$	$0.50L$	$0.40L$
Bike surfaces	$0.020 - 0.12L$	$0.013 - 0.09L$	$0.009 - 0.06L$
Number of inflation layers	4	10	20
y^+ of cyclist–bicycle	< 112	< 62	< 40
Element number (millions)	8	16	36

Lengths are normalised by the x hip location in the streamwise direction L.

accounting for turbulence. The continuity and momentum equations for the mean components are known as RANS equations and the additional Reynolds stress terms (involving cross-correlations of fluctuation components) that appear in these equations need to be modelled. The Boussinesq hypothesis is applied to model the Reynolds stress components in terms of the mean velocity gradient, basing the effectively turbulent viscosity on turbulence scales.[13]

The numerical solver, *ANSYS Fluent 18.0*, incorporates a conservative finite-volume method to solve the RANS equations. The pressure–velocity coupling scheme is used for these simulations. For the spatial discretisation, the velocity and pressure terms in the RANS equations were approximated to second-order accuracy. As recommended by Shur et al.,[14] $y^+ < 1$ was maintained for the first cell adjacent to the boundary surfaces to properly resolve the wall boundary layers. The boundary conditions applied to the domain boundaries and the placement of the cyclist in the domain are depicted in Figure 8, similar to the setup used by Griffith et al.[4]

The shear stress transport (SST) $k - \omega$ is a popular RANS model used to predict the flow in the near-wall region, as it is tailored to provide more accurate predictions in adverse pressure gradient regions. This model is a combination of the Wilcox $k - \omega$ model and the standard $k - \epsilon$ model.[15] These two formulations are blended in order to utilise the advantage of the superior near-wall treatment associated with the Wilcox $k - \omega$ model and the better outer layer stability of the $k - \epsilon$ model.

The TSST method was developed for transitional flows. It is a combination of SST $k - \omega$ model incorporating intermittency (γ) and the transition-onset Reynolds number (Re_θ) – the critical Reynolds number for the onset of intermittency.[16] Four transport equations need to be solved; the first two equations are similar to the SST $k - \omega$ equations.

Results and discussion

Body scan fidelity

To ensure the validity of the model, the dimensions of both the wind-tunnel setup and scanned model were recorded and compared – the key dimensions are shown in Table 1. Important factors that govern the drag force (F_D) are the frontal area (A) and the drag coefficient (C_D) given by equation (1)

$$F_D = C_D A \frac{1}{2} p U^2 \tag{1}$$

Since the frontal area is one of the important factors, the projected area was measured for both the wind-tunnel setup and CFD model, as shown in Figure 12. This was done by taking photographs of the setup of the cyclist/bicycle combination in the wind tunnel. The
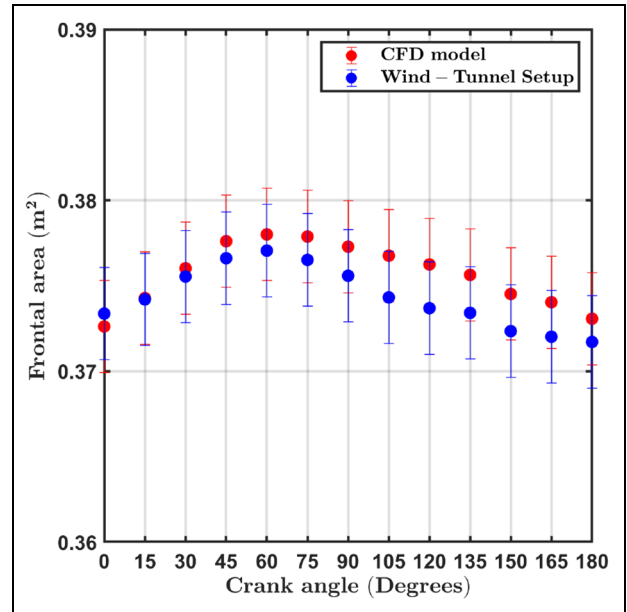

Figure 12. Variation of frontal area with crank angle.

photos were taken 10 m ahead of the model. Using a turquoise rectangular board at the back of the model, the background pixels were removed, followed by counting the pixels of the cyclist bicycle geometry (N_p). A reference area was placed at the mid point of the bicycle and the size of pixels (A_p) were read. Therefore, the total frontal area (A) was calculated by equation (2)

$$A = N_p \times A_p \tag{2}$$

For the CFD model, the frontal area was calculated after meshing, using the inbuilt area projection algorithm, which is nominally accurate to $\pm 0.0001 \, \text{m}^2$. The difference between the CFD and experimental frontal areas was $< 0.6\%$; this is a cumulative result of uncertainty with the scan and measurement of the number of pixels.

The validity of 3D scanning was tested by Seminati et al.[17] for anthropometric body parts such as the lower limb. To assess the accuracy, a comparison was made to a high resolution/precision scanner (Romer) with an accuracy of down to 0.04 mm, against 0.5 mm for the Artec Eva used for the current scanning. Based on the study, the cross-sectional areas on 20 planes were evaluated and the maximum error was found to be as high as 2%. However, in this study, the difference of the frontal area was found to be $\leqslant 0.6\%$.

There are several reasons for the slight variation in the frontal areas. To begin with, for the CFD simulations, the process requires minor simplifications of a highly complex model such as the cyclist/bicycle. These changes include smoothening of wrinkles on the suit; slight simplification of extrusions, such as nuts and bolts; and a generalisation of the representation of complex models as a bluff body, for instance, the

cranks and the chain-ring. In fact, not only during the model creation but also throughout the scanning process, there tend to be variations introduced. First, there are uncertainties in surface generation when individual scans are merged. Second, surface sections from different scans can (almost) overlap and this must be resolved. Finally, when the use of NURBS fitting creates a best fit smooth surface for the entire geometry, this depends on a fitting tolerance. Another source of variation is due to human judgement involved in the surface generation steps. Furthermore, hardware limitations of the scanner can also have an effect. For instance, it is likely that the scanner will not capture small features, such as, small crevices and holes.[18]

The importance of having a constant frontal area (and position) for athletes during wind-tunnel testing is important; researchers have reported difficulties in cyclists maintaining the same exact position during wind-tunnel testing.[11] In general, it is important to consider uncertainties in both experimental measurements and CFD predictions, as they can affect resistive forces. Previous RANS simulations have reported a variation of 12%–17% for drag[4,19] from experimental measurements and a contribution to this might be due to geometric differences. Consequently, a section of this article is devoted to documenting limitations in the process of scanning and producing a final model of the overall geometry.

The scanner, the Artec Eva, projects structured light on the desired scanned object. This structured light contains a series of patterns, which deform when they interact with a surface. The scanner's camera uses image recognition algorithms to determine the distance to the surface given the deformed light pattern. The 3D scanner can scan many objects well, but many challenges were faced to obtain a satisfactory scan of the cyclist/bicycle combination.

In practice, the most difficult objects to scan are those that are dark, shiny and transparent. Unfortunately, the bicycle/cyclist geometry contains all three, which causes a less than ideal scanning environment. These surfaces cause light distortion, such that it interferes with the data acquisition process. When a surface is clear, such as the wind shield of the helmet and other transparent surfaces, the light goes straight through the surface. Another factor is surface shininess, resulting in scattering of the light, which inhibits the process. Examples include the bicycle, helmet and reflective parts, such as raw metal components. Finally, dark surfaces are also problematic because of light absorption.

The bicycle was manufactured using carbon-fibre reinforced polymer held together by thermosetting epoxy resin. The resin is both partially reflective and transparent to the black carbon-fibre base below. To improve the surface properties for scanning, white anti-glare spray was used to cover the glossy surface finish
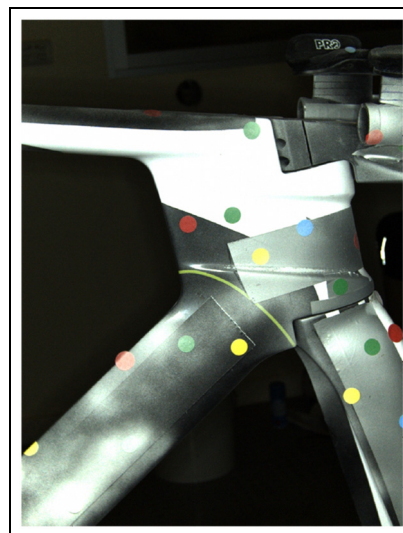

Figure 13. A photo of a section of the bicycle marked with reflective dots used for the scanning process using the Artec Eva scanner.

of the bicycle (Figure 13). However, it was found that this was not entirely adequate because of the difficulty of getting the spray to stick to the surfaces. As an added measure, 1-cm circular polka dot stickers were placed, as shown in Figure 13, which allowed more accurate surface detection.

Scanning the mannequin also had similar challenges involving the helmet windshield and inner thighs. To get a good scan of the windshield, it was necessary to cover it with an anti-glare spray supplemented with the coloured dots. Despite this, the scanner still had difficulty picking up the reflected light pattern. The solution was to dim the lights that were directly facing the top of the cyclist, finally resulting in a satisfactory helmet scan. For the thighs, the scanner's light had difficulty properly accessing the region between the thighs. However, use of an elevated setup enabled a good scan to be obtained from below. For this article, all scans were taken using the AS-10 software. However, subsequently, the same setup was tested with the newer version of the software *Artec Studio 12* (AS-12); this resulted in much better scans. In fact, the shiny surfaces were captured with minimal effort due to improvements in the reconstruction algorithm.

The alignment for the scanned surfaces was done manually using the AS-10 software by picking reference points between pairs of surface scans. For example, three to four dots recognised in both scans could be used for surface alignment. This manual process tends to be long and tedious. There is an alternative automatic procedure built into the package to automatically join the separate surfaces together. Unfortunately, this process has a high computational cost, taking 4–5 days on a personal computer with 64 Gb RAM. However, in
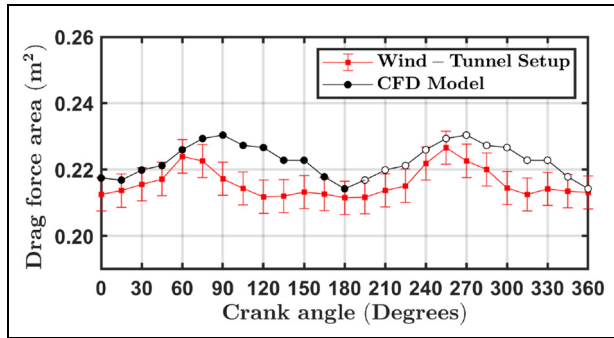
Figure 14. Variation of drag force area against crank angle. Open circles show CFD drag force area assuming symmetry.

the newer version of the software (AS-12), the process takes $\leqslant 1$ h to scan and ≈ 4 h to process the data. Thus, this becomes a much more workable option.

The whole process is summarised in Figure 4, from the initial scanned surfaces, merging and cleaning up. The initial scan generates a triangular surface mesh that needs to be coarsened for efficiency before converting it to a NURBS representation (Figure 5). The initial scanned object consisted of nearly 1.6 million cells. Open-source software, *Mesh-mixer*, was used to patch and reduce the number of facets, while still ensuring that it was sufficient to accurately represent the surface. This surface object was subsequently converted to NURBS for two main reasons: (1) better control of the model to add in the pedals, cranks and wheels, and (2) computational efficiency, since a lot of the computer RAM was needed just to store the model. Finally, the complete CAD surface model was aligned in the *x, y, z* coordinate system for the CFD simulation; this was done in *SolidWorks*. (The parameterised moving-leg model can be seen by clicking, *dynamic cyclist model*).

Numerical model

To provide validation of the numerical model, predictions are compared with experimental measurements for the drag-area. This comparison is shown in Figure 14. The numerical simulations capture the general trend of the drag with pedal position, over-predicting the drag by $\leqslant 1\%$–7% across the cycle. One reason for this over prediction may be due to the numerical model not accurately capturing the effect of surface roughness of the skin suit. Surface roughness can result in a drag reduction in the drag crisis region by $\sim 50\%$ for cylindrical bodies.[20] If the drag contribution of the arms is nominally reduced by a similar factor, the difference in the drag drops to $\leqslant 5\%$.

There are simlar numerical studies on cyclists. Defraeye et al.[19] reported a variation of 12%–13% for their RANS study based on the $k - \epsilon$ turbulence model. Another study by Griffith et al.[4] reported 13%–17% variation in drag for a RANS numerical

simulation using the SST $k - \omega$ turbulence model, but on a simplified cyclist. This simulation was conducted using scanned athletes and considerable care has been taken to produce an accurate model. In this study, the reported variation is less than $\sim 7\%$ for the TSST RANS model, which is significantly closer to the experimental result. This is likely due to both using a more appropriate turbulence model and having a more accurate CAD model. Recent studies by Blocken et al.[8] confirms the benefits of TSST for cycling applications.

Beyond these issues, however, there is a further limitation to precise predictions based on RANS modelling. In the current instance, the geometry is treated as a smooth surface, while suit surface roughness does certainly affect the drag contribution from different parts of a cyclist. Surface roughness can be included in the RANS model, but to get accurate drag predictions requires high-fidelity prediction of laminar to turbulence transition together with small separation regions, especially on the arms. The use of the transitional SST model helps, but it is unlikely that it will faithfully reproduce actual separation lines on critical parts of the cyclist subject to differing surface textures. Nevertheless, the simulations can be very useful to predict larger scale flow features and general separation and reattachment to aid with aerodynamic optimisation.

A significant drag variation between the low- and high-drag pedal phase angle is observed in both the wind tunnel and CFD of $\sim 7\%$; a similar (but larger) variation was seen previously in the work by Crouch[21] ($\sim 15\%$), based on a slightly different cyclist position, head position and suit, and also the work of others. For the CFD simulations, some minor simplifications were made to the crank and pedals to achieve a simpler design. Furthermore, some inaccuracy may result from inadequacies with RANS turbulence modelling. It is likely that better predictions may be achieved using a more computational expensive time-dependent model, such as LES or variants of it.
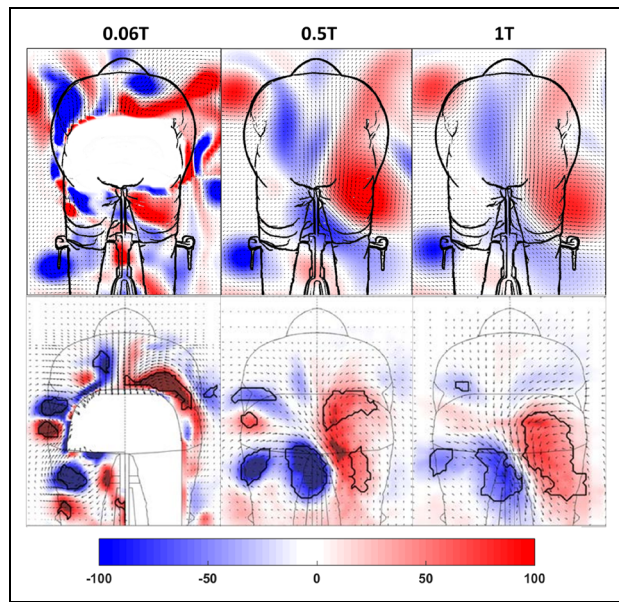
As mentioned above, the overall drag variation over the pedal stroke is $\sim 7\%$ for both the wind-tunnel measurements and simulations (Figure 14). In the experiments, the drag-area remained approximately constant between $300°$ and $15°$ and $120°$ and $210°$ at a value of $C_{D,A} \sim 0.210 - 0.215$. Between these ranges, there are gradual increases and decreases, with local maxima of ~ 0.225 occurring at $60°$–$75°$ and $\sim 225°$. The general variation observed for the CFD simulations is similar, but with the local maxima occurring closer to $90°$. From this angle, the drag-area decreases almost linearly to give predictions very close to the experimental values at $0°$ and $180°$. Overall, since the frontal area variation with respect to crank angle is $< 2\%$, variation in the drag coefficient must be mainly responsible for the variation in drag-area, as was also observed by Crouch et al.[10]

For the CFD, a side-by-side comparison of the downstream wake evolution between simulation
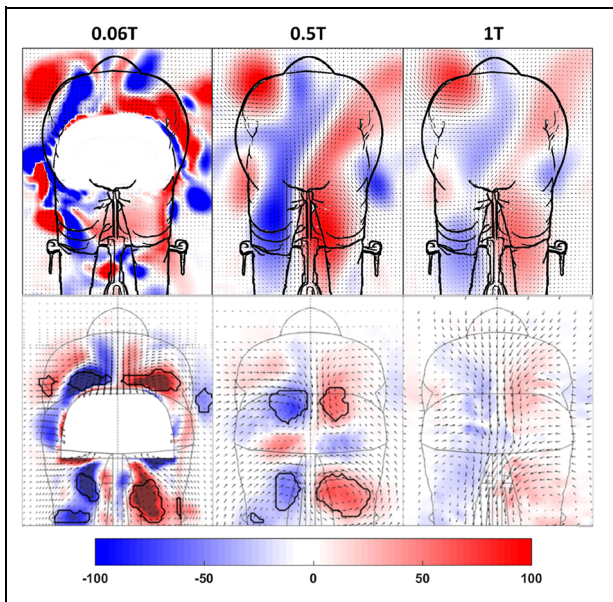
Figure 15. Variation of streamwise vorticity with the downstream position with the cross-plane position marked. Blue represents clockwise and red anti-clockwise vorticity. The bottom image shows the vorticity distributions from previous experiments but for a cyclist in a slightly different position and for a different suit[10] at $-0.06T$, $0.5T$ and T. These images correspond to the $15°$ (low drag) crank position.


Figure 16. Variation of streamwise vorticity with the downstream position with the cross-plane position marked. Blue represents clockwise and red anti-clockwise vorticity. The bottom image shows the vorticity distributions from previous experiments but for a cyclist in a slightly different position and for a different suit[10] at $-0.06T$, $0.5T$ and T. These images correspond to the $75°$ (high drag) crank position.

predictions and experimental measurements[10] depicted by vorticity is shown in Figures 15 and 16 at positions $-0.06T$, $0.5T$ and T for both high- and low-drag crank positions (Figure 17). The vorticity contours were compared with those of Crouch et al.[10] derived from wind-tunnel velocity measurements in downstream planes taken using a Cobra Probe. The latter measurements were obtained for a slightly different setup using a different bicycle, slightly altered back position, different skin suit and more upright head position – compare Table 1 of this article and Figure 3 of Crouch et al.[10] The experimental results are shown for a subset of the numerical planes: $-0.06T$, $0.5T$ and T downstream from the rear of the cyclist. Importantly, the images show the more symmetrical pattern of the low-drag case, together with the lower downstream vorticity level. Since these vortex structures may be associated with energy losses, this is consistent with the reduced drag when the legs are in the more symmetrical position (with thighs aligned and approximately horizontal). For the high-drag set-up, the comparison of the vorticity highlights the wake asymmetry, both in numerical predictions and the experiment by Crouch et al.[10] Beyond the structures observed in experiments, it depicts two additional elbow vortex structures. This is likely due to the cyclist/bicycle setup where the elbow joint angle is different by $10°$. Beyond this, there are similarities and differences between the wake cross-sections for simulations and experiments. It is envisaged that a more complex time-dependent CFD model, such
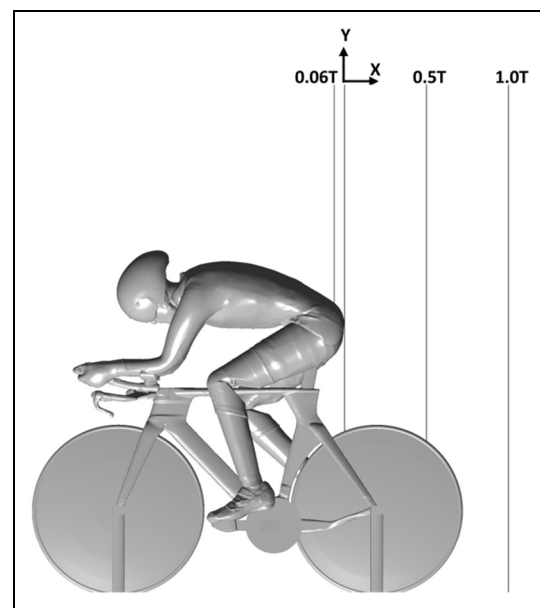
Figure 17. Downstream locations at which the velocity variation was recorded.

as LES, would produce a closer fit to the wake vortex structures, although it should be remembered that both the cyclist and bicycle are different between the experiments and the simulations.

To further understand the flow around the geometry, the horizontal velocity variation in the horizontal
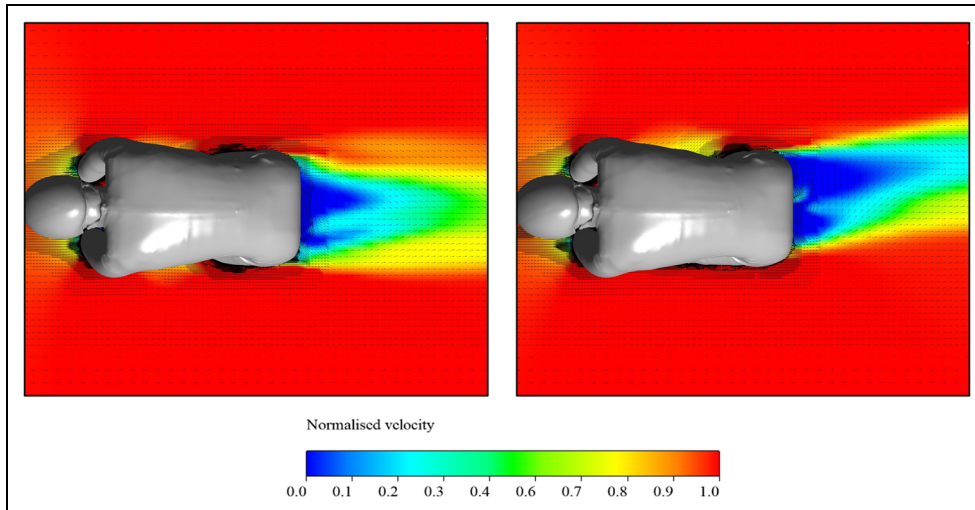
Figure 18. The left and right figures show the horizontal velocity distribution in a plane at the top of the seat-post for the low- and high-drag crank angle cases, respectively.

plane located through the top of the seat post is shown in Figure 18. For the high-drag crank angle, a strong velocity deficit can be observed compared with that at the low-drag position. Furthermore, the asymmetry can be clearly seen in the high-drag case with the wake angled strongly to one side. In contrast, the low-drag case shows a near symmetrical profile. For the high-drag position, the extended leg results in a large and nonsymmetric velocity deficit. The majority of the variation occurs below the hip of the cyclist. This is a by product of the flow separation from the hip, thighs and lower back. A symmetrical flow regime is observed when the flow separates evenly across the lower back, forming a large wake on top of the hip as shown in Figure 15. The asymmetrical flow features are a result of flow separation from the left and right side of the hips. In this regime, the flow separates earlier on the extended leg, while in the raised leg position, the flow remains relatively attached on the side of the thigh.

The resistive force contributions were monitored for body and bicycle components (see Figure 19) to determine the importance of each contribution to the overall drag. This breakdown of drag into component contributions is given in Figures 19 and 20. Although the interactions between the elements are nonlinear, this still provides information of specific areas to target to reduce overall drag, such as surface treatments or positional changes for the cyclist, or geometry changes for the bicycle. The bicycle and cranks produce a similar trend to the total drag variation found in both wind-tunnel tests and simulation predictions. However, the wheels show the opposite trend, a drop to lower value and then a rise. The other sub-body components, such as the stands, front wheel, handlebars, shoes and wrists, show a much smaller variation with respect to crank angle. Interestingly, the drag changes for the torso, cog and seat-post over the crank angle appears to

show more complex variation, as shown in Figures 19 and 20. Certainly, the ability of the CFD simulations to provide this detailed breakdown of drag contributions is well beyond the capability of experimental techniques at present.

This information is summarised in Table 3. The resistive force contributions to the high- and low-drag crank angle cases were broadly grouped into three sets: upper body, lower body, and bicycle components, as shown in Table 3. This shows that there is not much difference between the contributions to overall drag from each of these groups between the low- and high-drag cases. In terms of absolute contributions, the bike components and lower-body sets result in drag increases of 7% and 11%, respectively, while the upper body appears to have a negligible effect ($< 1\%$). However, examination of the contributions from individual components, also shown in the table, indicates that the leg and crank positions are the main contributors to the change. The alignment of one thigh and the cranks across the flow in the high-drag case changes the contribution of those components by 9% between the two cases. A similar conclusion was reached by Crouch et al.[10] using a simplified model of the effect of leg position on overall drag.

Overall, the upper body is the main contributor to the overall drag (44%–42%), followed by the lower body (35%–37%), for low- and high-drag crank-angle cases, respectively.

Conclusion

This article describes a process of obtaining an accurate surface description of the surface of a cyclist/bicycle combination from a body scan. Available existing software also provides an ability to segment the geometry into different identifiable components (such as the head, arms, thighs, etc.), allowing a determination of
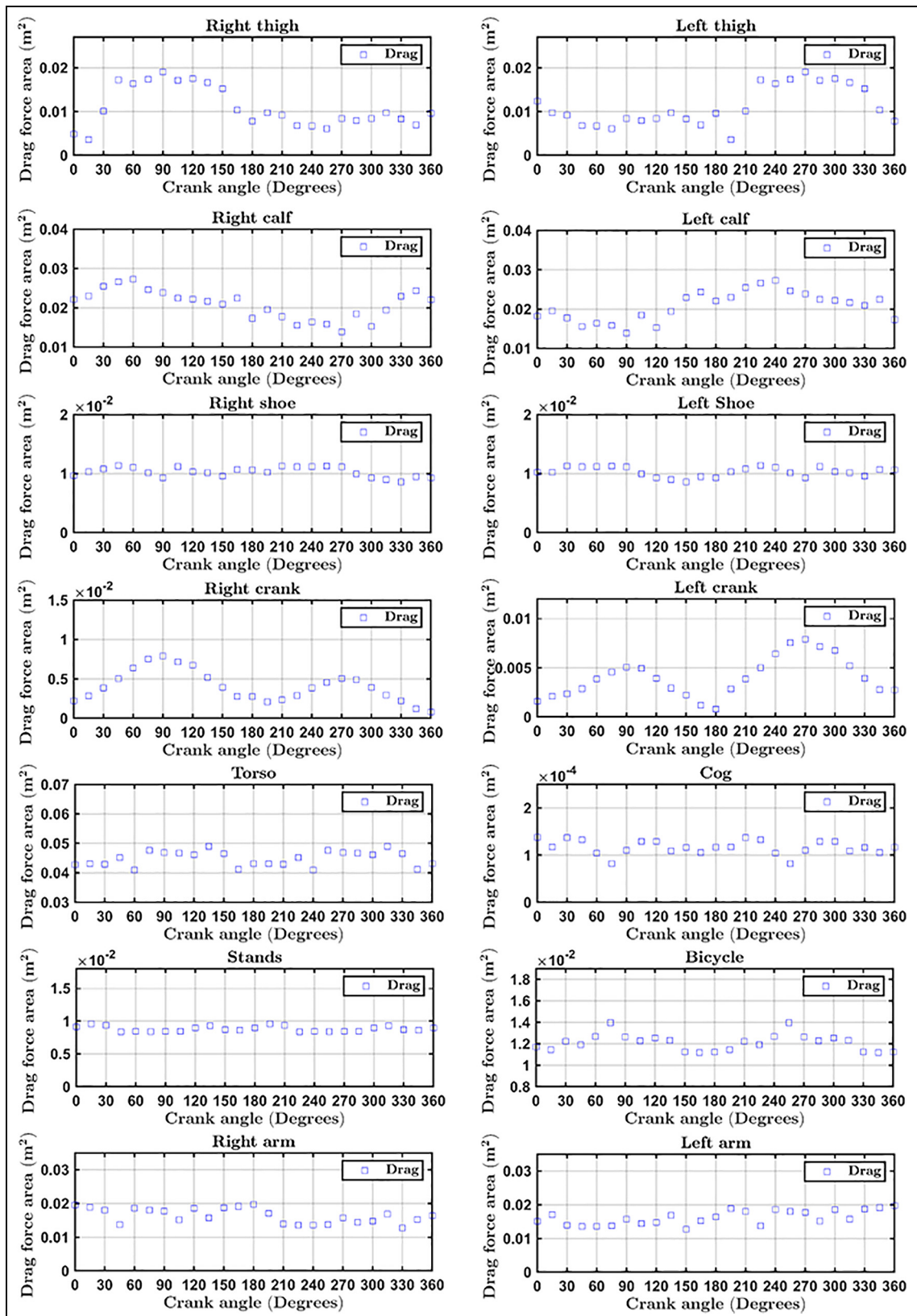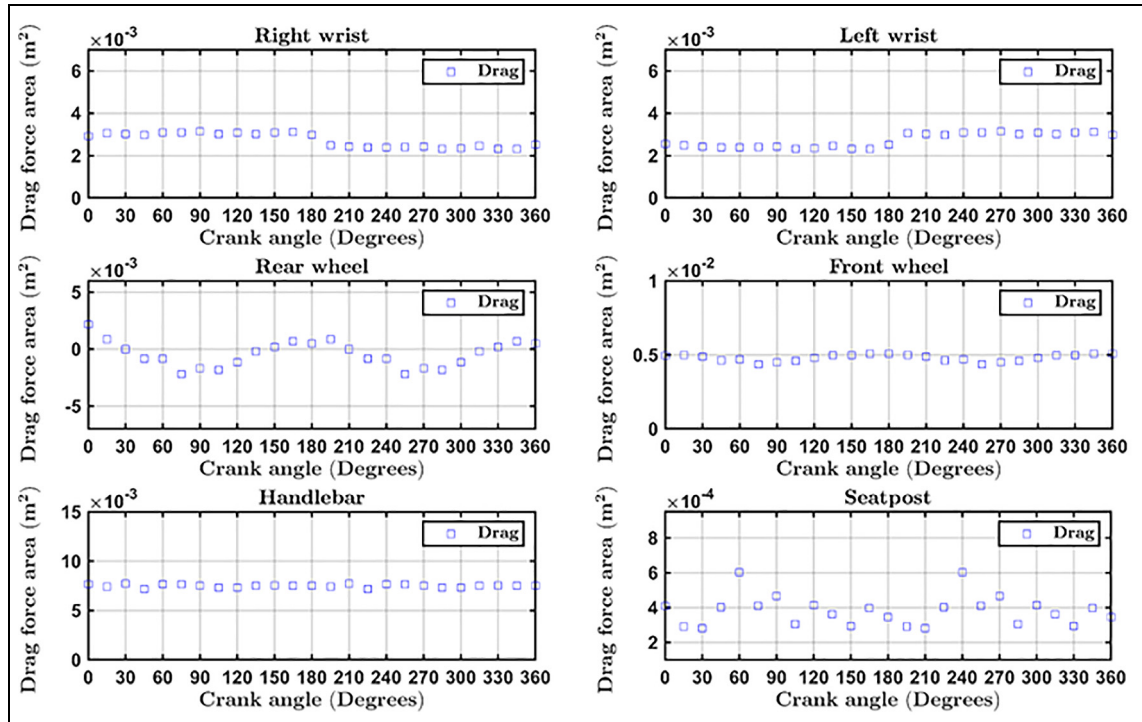
Figure 19. Drag force area for sub body components for cyclist-bicycle combination.

the contribution to the overall aerodynamic drag of each component.

An advantage over using experiments to obtain aerodynamic force is the detailed breakdown of drag in

terms of contributions from separate components possible with CFD simulations. For the CFD study, the cyclist/bicycle was segmented into 23 components. Examination of the drag from these components

Figure 20. Drag force area for sub body components for cyclist-bicycle combination.

provides the following information for the variation over a pedalling cycle:

- The bicycle and cranks produce a total drag variation similar to the wind-tunnel experiment and numerical simulation: a rise and then a drop to a lower value.
- In contrast, the wheels shows an opposite trend with respect to the total drag: a drop to a lower value and then a rise.
- The remaining sub-body components, such as the stands, front wheel, handlebars and shoes, show only relatively small variations with respect to crank angle.

The low- and high-drag crank angles (15° and 75°) produce an almost symmetrical and asymmetrical wake structure. Although this has been previously reported, a thorough comparison between sub-body contributions has not been presented before. The important variations have been highlighted as follows:

- The main change in drag between these two positions for the sub-parts was reported on the thighs. For the right thigh, the contribution was 383% higher when compared with the lower drag angle value. In contrast, the left thigh contribution varied by –38%. This is in fact mainly due to the increased frontal area of the extended leg, and vice versa for the contracted left thigh.
- The right and left crank reported drag increases of 163% and 118%, respectively, when compared with

the drags at the lower drag angle. This is in fact due to the extended position resulting in the increased frontal area.

- For the main body parts, relative to the low-drag angle case, the upper body has a small variation in drag resulting in a –1% change, while the lower body and the bicycle components had a more significant variation, comprising 11% and 7%, respectively. These results are depicted in Table 3.

Another important contribution of this article is the documentation of the detailed procedure and limitations involved in experimental testing, body scanning and numerical simulations. Although previous numerical simulations have been conducted based on body scans, it is useful to detail the limitations involved in such a process.[8,19,22–25] The investigation highlights the uncertainties involved in scanning, which can affect the overall volume, and therefore the frontal area. Therefore, part of this case study developed a procedure for validating the scanning process for future numerical simulations.

Furthermore, from a single scan of a cyclist in a fixed position, it is possible to form a deformable model that has moving legs, allowing simulations at different phases of the pedalling cycle. This approach was used to provide the geometry for resolved 3D numerical simulations over 180° of the crank cycle at 15° increments using the time-mean RANS TSST model on a 36 million cell mesh. The predictions from this model were cross-validated against wind-tunnel tests of the same mannequin/bicycle combination. The

Table 3. Top: relative contribution to the overall aerodynamic drag from different body and bicycle component groups; bottom: drag contributions from the different groups for the low- and high-drag cases, and the percentage change in drag for the high-drag case relative to the low-drag crank-angle case.

Body part	Low drag 15°	High drag 75°	
Torso	20	21	
Right thigh	2	8	
Left thigh	4	3	
Right crank	1	3	
Left crank	1	2	
Bicycle components	21	21	
Upper body	44	42	
Lower body	35	37	
Body part	Low drag 15° (m^2)	High drag 75° (m^2)	% rise in drag respect to 15° crank
Torso	0.0431	0.0475	10
Right thigh	0.0036	0.0174	383
Left thigh	0.0097	0.0061	−38
Right crank	0.0029	0.0075	163
Left crank	0.0021	0.0045	118
Bicycle components	0.0452	0.0484	7
Upper body	0.0963	0.0957	−1
Lower body	0.0765	0.0852	11

Component groupings consist of (1) bicycle components: cranks, handlebars, pedals, stands, seat post, front and rear wheels and cog; (2) upper body: arms, torso, head and wrists; and (3) lower body: calves, thighs and shoes.

wind-tunnel measurements show a variation in drag over the pedalling cycle of approximately 7%, with high drag recorded for the case with one leg fully extended and low drag corresponding to when both thighs are approximately horizontal. The numerical prediction of the aerodynamic drag variation matched that of experiments reasonably well, with a variable difference of +1–7% over the cycle. In addition, the simulated time-mean vortical wake structures show reasonable agreement with previous wake measurement for a similar cyclist/bicycle setup. In particular, a much higher wake velocity deficit and stronger streamwise vortical structures are observed for the high-drag case. It was speculated that the increase in the predicted drag over direct experimental measurements may have been due, at least partially, to surface texture of the mannequin skin suit, which may have resulted in a drag reduction for body components, such as the arms, given that the local Reynolds number is close to the drag crisis region. This aspect needs further exploration, together with extending the modelling to employ more complex unsteady methods, such as variants of detached eddy simulation, which are generally observed to produce more accurate representations of the mean wake structure. Finally, the inclusion of leg motion provided by this model can also allow the influence of dynamic pedalling on the flow to be assessed through future time-dependent moving mesh simulations.

ORCID iDs

Shian Chi https://orcid.org/0000-0001-6366-4195
Tim Crouch https://orcid.org/0000-0001-8208-0101

References

1. Grappe F, Candau R, Belli A, et al. Aerodynamic drag in field cycling with special reference to the Obree position. *Ergonomics* 1997; 40(12): 1299–1311.
2. Kyle CR and Weaver MD. Aerodynamics of human-powered vehicles. *Proc IMechE, Part A: J Power and Energy* 2004; 218(3): 141–154.
3. Kyle CR and Burke E. Improving the racing bicycle. *Mech Eng* 1984; 106(9): 34–45.
4. Griffith MD, Crouch T, Thompson MC, et al. Computational fluid dynamics study of the effect of leg position on cyclist aerodynamic drag. *J Fluid Eng* 2014; 136(10): 101105.
5. Underwood L. *Aerodynamics of track cycling*. PhD Thesis, Department of Mechanical Engineering, University of Canterbury, Christchurch, New Zealand, pp.36–37, 2012.
6. Underwood L and Jermy MC. Fabric testing for cycling skinsuits. *Procedia Eng* 2011; 13: 350–356.
7. Defraeye T, Blocken B, Koninckx E, et al. Computational fluid dynamics analysis of cyclist aerodynamics: performance of different turbulence-modelling and boundary-layer modelling approaches. *J Biomech* 2010; 43(12): 2281–2287.
8. Blocken B, van Druenen T, Toparlar Y, et al. Aerodynamic drag in cycling pelotons: new insights by CFD simulation and wind tunnel testing. *J Wind Eng Indus Aerodyn* 2018; 179: 319–337.
9. Blocken B, Defraeye T, Koninckx E, et al. CFD simulations of the aerodynamic drag of two drafting cyclists. *Comput Fluid* 2013; 71: 435–445.
10. Crouch TN, Burton D, Brown NAT, et al. Flow topology in the wake of a cyclist and its effect on aerodynamic drag. *J Fluid Mech* 2014; 748: 5–35.
11. Barry N, Burton D, Sheridan J, et al. Aerodynamic drag interactions between cyclists in a team pursuit. *Sport Eng* 2015; 18(2): 93–103.
12. Langtry RB, Menter FR, Likki SR, et al. A correlation-based transition model using local variables II: test cases

and industrial applications. *J Turbomach* 2006; 128(3): 423–434.

13. Schmitt FG. About Boussinesq's turbulent viscosity hypothesis: historical remarks and a direct evaluation of its validity. *Comptes Rendus Mécanique* 2007; 335(9–10): 617–627.

14. Shur ML, Spalart PR, Strelets MK, et al. A hybrid RANS-LES approach with delayed-DES and wall-modelled LES capabilities. *Int J Heat Fluid Flow* 2008; 29(6): 1638–1649.

15. Versteeg HK and Malalasekera W. *An introduction to computational fluid dynamics: the finite-volume method.* Pearson Education, 2007.

16. Menter FR, Langtry RB, Likki SR, et al. A correlation-based transition model using local variables I: model formulation. *J Turbomach* 2006; 128(3): 413–422.

17. Seminati E, Talamas DC, Young M, et al. Validity and reliability of a novel 3D scanner for assessment of the shape and volume of amputees' residual limb models. *PLoS ONE* 2017; 12(9): e0184498.

18. Michaeli JG, DeGroff MC and Roxas RC. Error aggregation in the reengineering process from 3D scanning to printing. *Scanning* 2017; 2017: 1218541.

19. Defraeye T, Blocken B, Koninckx E, et al. Aerodynamic study of different cyclist positions: CFD analysis and full-scale wind-tunnel tests. *J Biomech* 2010; 43(7): 1262–1268.

20. Zdravkovich MM. *Flow around circular cylinders: Applications*, vol. 2. Oxford: Oxford University Press, 1997.

21. Crouch T. *Flow topology and large-scale wake structures around elite low-drag cycling positions.* PhD Thesis, Department of Mechanical Engineering and Aerospace Engineering, Monash University, Melbourne, VIC, Australia, pp.81–132, 2013.

22. Blocken B and Toparlar Y. A following car influences cyclist drag: CFD simulations and wind tunnel measurements. *J Wind Eng Indus Aerodyn* 2015; 145: 178–186.

23. Defraeye T, Blocken B, Koninckx E, et al. Computational fluid dynamics analysis of drag and convective heat transfer of individual body segments for different cyclist positions. *J Biomech* 2011; 44(9): 1695–1701.

24. Defraeye T, Blocken B, Koninckx E, et al. Cyclist drag in team pursuit: influence of cyclist sequence, stature, and arm spacing. *J Biomech Eng* 2014; 136(1): 011005.

25. Mannion P, Toparlar Y, Clifford E, et al. On the effects of crosswinds in tandem aerodynamics: an experimental and computational study. *European J Mech-B/Fluid* 2019; 74: 68–80.